Steel and Composite Structures, *Vol. 56, No. 5 (2025) 365-374*
https://doi.org/10.12989/scs.2025.56.5.365

Evaluation of rutting depth in unpaved roads using electromagnetic wave techniques

Seonghun Kang[1a], Geunwoo Park[1b], Seungjun Kim[1c], Thomas H.-K. Kang[2d] and Jong-Sub Lee[*1]

[1]*School of Civil, Environmental and Architectural Engineering, Korea University, Seoul 02841, Korea*
[2]*Department of Architecture & Architectural Engineering, Seoul National University, Seoul 08826, Korea*

(Received April 25, 2025, Revised June 19, 2025, Accepted June 24, 2025)

Abstract. This study evaluates the applicability of ground penetrating radar (GPR) and time domain reflectometry (TDR) for assessing rutting depth on unpaved roads. A testbed is constructed using sandy soil, and vehicular loading is applied through repeated passes of a dump truck (0, 100, 200, and 500 times). The rutting depth is estimated based on the travel time extracted from the GPR images and permittivity values obtained from the TDR measurements. The accuracy of these estimates is compared with the results of dynamic cone penetrometer (DCP) tests. Additionally, the rutting depth estimated by GPR analysis is compared with the values obtained using the conventional straightedge method. The results indicate that incorporating GPR with TDR enables accurate estimation of subsurface interface depths. Moreover, while conventional methods tend to underestimate the rutting depth owing to the deformation of the reference surface, the GPR-based analysis shows minimal error from such deformation. This study demonstrates that GPR and TDR can be powerful tools for evaluating the rutting depth across an entire road cross section.

Keywords: ground penetrating radar; relative permittivity; rutting depth; time domain reflectometry; unpaved road

1. Introduction

Most roads in South Korea are paved; however, unpaved roads are commonly found in mountainous areas and regions designated for military operations (Korea Transport Institute 2019, MOLIT of Korea 2021). These unpaved roads tend to experience greater reductions in operational efficiency, safety, and user convenience compared to paved roads (Kim *et al*. 2025, Ramjiram *et al*. 2021). The bearing capacity of unpaved roads is primarily determined by soil conditions, including water content and relative density. When the stress caused by vehicular loading exceeds the soil's capacity, shear failure occurs along the periphery of the loaded zone. Furthermore, increased water content in the soil resulting from rainfall reduces the shear strength of the ground, thereby facilitating the occurrence of shear failure under repeated traffic loading (Hausmann 1987, Heidari *et al*. 2022). Accordingly, unpaved roads exhibit greater vulnerability to declines in serviceability and stability than paved roads. As rebuilding costs tend to exceed maintenance expenses, it is essential to accurately evaluate the condition of unpaved roads, particularly within the upper few meters of soil (Eaton 1992).

Conventional site investigation methods for evaluating the serviceability of unpaved roads emphasize the surface conditions (Abbondati *et al*. 2021). A widely used system is the Pavement Surface Evaluation and Rating (PASER) scale introduced by the Wisconsin–Madison Transportation Information Center. The PASER scale assigns scores from 1 (failed) to 5 (excellent) based on criteria, such as the surface deformation, crown shape, drainage efficiency, gravel layer condition, and visible defects (Aleadelat *et al*. 2018). Similarly, the U.S. Army Corps of Engineers established the Unsurfaced Road Condition Index (URCI), which evaluates surface-related issues, including ruts, potholes, inadequate cross sections, poor drainage, corrugations, dust, and loose aggregates (Eaton 1992, Soria and Fontenele 2003). Accordingly, the rutting depth is consistently recognized as an important parameter that influences the serviceability assessments of unpaved roads. Thus, an accurate evaluation of rutting depth is essential for the effective maintenance of unpaved roads.

Various methods have been proposed for measuring the rutting depth. ASTM E1703 (2010) introduced a method using a straightedge as follows: the straightedge was first placed across the crests on both sides of the rut, as shown in Fig. 1, and then the perpendicular distance (d_r) from the straight edge to the road surface was measured. During this process, a straightedge was maintained perpendicular to the traffic direction. However, this method is limited in that it captures only the maximum rutting depth and does not provide information on the extent of structural stability degradation across the entire road cross section. Wang *et al*. (2017) and Hui *et al*. (2018) proposed a method for estimating the rutting depth by emitting laser beams onto the road surface and measuring the reflected signals to determine the relative depth differences across the road

*Corresponding author, Ph.D. Professor
E-mail: jongsub@korea.ac.kr
[a]Ph.D. Research Professor
[b]Ph.D. Post Doctoral Researcher
[c]Ph.D. Associate Professor
[d]Ph.D. Professor

ISSN: 1229-9367 (Print), 1598-6233 (Online)

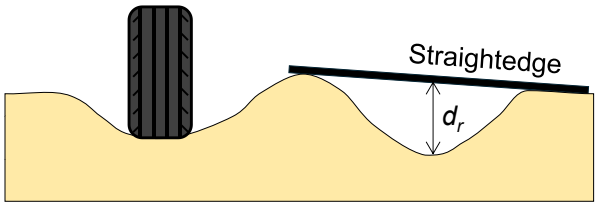

Fig. 1 Rut depth measurement

*d_r: rutting depth

cross section. However, this approach, which is based on relative depth measurements, is limited because it cannot adequately account for the ground deformation occurring across the entire road cross section.

To ensure a reliable evaluation of unpaved road conditions, a precise assessment of the absolute deformation throughout the entire cross section in the upper few meters is necessary. Recently, nondestructive geophysical survey methods that utilize electromagnetic, elastic, and acoustic waves have been widely applied to evaluate extensive target areas of social infrastructure facilities without the need for intrusive testing (Kang *et al*. 2021, Kang *et al*. 2025a). Ground penetrating radar (GPR) surveys operate by emitting electromagnetic waves into the ground and measuring the reflected signals at interfaces where significant contrasts in permittivity occur between subsurface layers. GPR surveys are time-efficient and nondestructive, allowing the assessment of entire unpaved roads without disturbing the upper layers, making them a potentially effective method for evaluating the rutting depth. Additionally, time domain reflectometry (TDR), which utilizes electromagnetic waves to assess the permittivity of materials, can be applied to soils to estimate their relative permittivities. This information can significantly improve the accuracy of the GPR signal interpretation when evaluating subsurface conditions (Kang *et al*. 2023, Kang *et al*. 2024).

This study investigated the distance from the surface of an unpaved road to the underlying ground layers across the entire cross section of the road, which is considered the rutting depth, using GPR and TDR. Rutting depths were measured under various numbers of repeated vehicle loads. The results of the rutting depth measurements were compared with those obtained using a dynamic cone penetration (DCP) test and a conventional method. In addition, we discuss the fundamental principles of GPR surveys, TDR measurements, and DCP testing, followed by the experimental procedures and results for each method. Based on these findings, a novel approach is proposed to evaluate the serviceability and structural stability of unpaved roads using electromagnetic wave-based techniques.

2. Theoretical background

2.1 Ground penetrating radar (GPR)

GPR surveys enable the identification of subsurface interfaces characterized by variations in electromagnetic

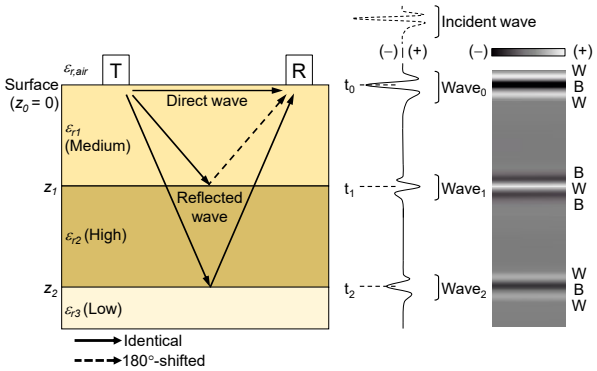

Fig. 2 Reflection of electromagnetic waves by subsurface anomalies

impedance (Davis and Annan 1989, Annan 2003, Jia *et al*. 2022). The system emits electromagnetic waves into the ground and interprets the waves reflected by subsurface anomalies, as illustrated in Fig. 2 (Annan 2003, Kang *et al*. 2022). The electromagnetic impedance z^* of a medium is defined as the ratio between the electric and magnetic field components, and can be described by the following relationship (Santamarina *et al*. 2001):

$$z^* \propto \frac{c}{\sqrt{\varepsilon_r}} \tag{1}$$

As the velocity c of electromagnetic waves in a vacuum is constant ($c \approx 3.0 \times 10^8$ m/s), the impedance z^* becomes inversely proportional to the square root of the medium's relative permittivity ε_r (Eq. (1)). The reflection coefficient R^*, defined at an interface between two media, is governed by the contrast in their electromagnetic impedances and expressed as follows (Hong and Lee 2018, Kim *et al*. 2024):

$$R^* = \frac{-{z_1}^* + {z_2}^*}{{z_1}^* + {z_2}^*} = \frac{\sqrt{\varepsilon_{r1}} - \sqrt{\varepsilon_{r2}}}{\sqrt{\varepsilon_{r1}} + \sqrt{\varepsilon_{r2}}} \tag{2}$$

where ${z_1}^*$ and ${z_2}^*$ refer to the impedance of the upper and lower layers, respectively, and ε_{r1} and ε_{r2} correspond to their relative permittivities (Fig. 2). The sign of R^* determines whether the reflected signal has the same or opposite polarity as the incident wave (Jiao *et al*. 2020).

In this study, the GPR images were visualized using a grayscale scheme, wherein positive polarity is denoted by white (W) and negative polarity by black (B). The polarity pattern of the reflected signal, such as W–B–W or B–W–B, can be effectively distinguished based on the sign of the second half-cycle of the waveform. The first waveform, $Wave_0$ in Fig. 2, corresponds to a direct wave traveling from the transmitter dipole (T) to the receiver dipole (R) (Annan 2003). During the propagation of a direct wave, the wave does not encounter any interface to be reflected off, and its polarity remains the same as that of an incident wave. Thus, the W–B–W polarity of the direct wave was set as a reference for polarity comparison in this study. In the case of $\varepsilon_{r1} < \varepsilon_{r2}$, the sign of R^* is negative (Eq. (2)), and the reflected signal had a 180°-shifted polarity relative to the incident wave ($Wave_1$ in Fig. 2). Conversely, when $\varepsilon_{r1} > \varepsilon_{r2}$, the R^* becomes positive, resulting in the same polarity relative to the incident wave ($Wave_2$ in Fig. 2) (Kang *et al*. 2025b).

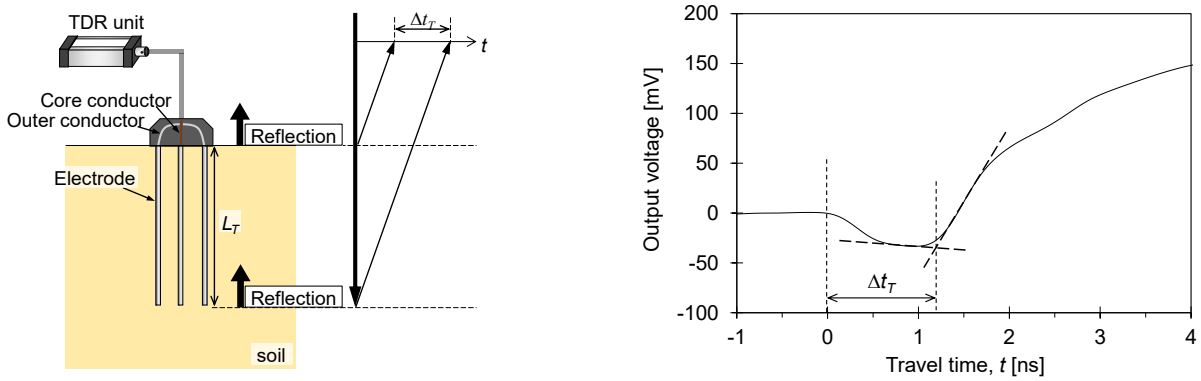

(a) TDR system (b) TDR signal

Fig. 3 Schematic drawing of TDR measurement and signal

The interface depth d can be derived using the wave velocity v, travel time t of the reflected signal, and the ε_r value of the ground, as follows:

$$d = v \cdot \frac{t}{2} = \frac{ct}{2\sqrt{\varepsilon_r}} \tag{3}$$

To determine the travel times for both the direct and reflected waves, the peak of the second half-cycle of each waveform was used as a reference point (Yelf 2004). In the case of ground-coupled antennas, the travel time of the direct wave was considered to be equivalent to a depth of $z = 0$. Accordingly, the depth to the subsurface interface was computed by aligning all reflected wave travel times relative to the direct wave (0 ns), as illustrated in Fig. 2.

2.2 Time domain reflectometry (TDR)

The TDR method was applied to evaluate the relative permittivity of the in situ soil (ASTM D6565 2005, Hong *et al*. 2016). This method operates by emitting guided electromagnetic waves along transmission lines and recording the reflections that occur at dielectric discontinuities. Because the electromagnetic impedance varies across different media, the wave travel time is affected accordingly (Fig. 3(a)). The ε_r value of the surrounding medium was determined using the following equation:

$$\varepsilon_r = \left(\frac{c}{v}\right)^2 = \left(\frac{c\Delta t_T}{2L_T}\right)^2 \tag{4}$$

where L_T is the length of the TDR probe (75 mm in this study), and Δt_T is the interval of travel time for the electromagnetic waves reflected at both TDR probe ends (Fig. 3(a)). The value of Δt_T was obtained by calculating the time interval between the initial and final inflection points of the measured TDR signals (Fig. 3(b)). The tangent method was employed to capture inflection points (Klemunes 1998).

2.3 Dynamic cone penetrometer (DCP)

The DCP test evaluates ground strength by measuring the penetration depth of a small-scale penetrometer subjected to impact loading (Scala 1956, Hong *et al*. 2018). The DCP apparatus comprises a hammer weighing 78.4 N, an anvil, driving rods with a diameter of 16 mm, and a cone tip with a diameter of 20 mm and an apex angle of 60°, as illustrated in Fig. 4. As shown in Fig. 4, penetration can be achieved through repeated freefall impacts, where the hammer is released from a height of 575 mm. In this study, the number of hammer blows and the corresponding penetration depths were recorded to determine the dynamic cone penetration index (DCPI) in mm/blow units, following ASTM D6951 (2009):

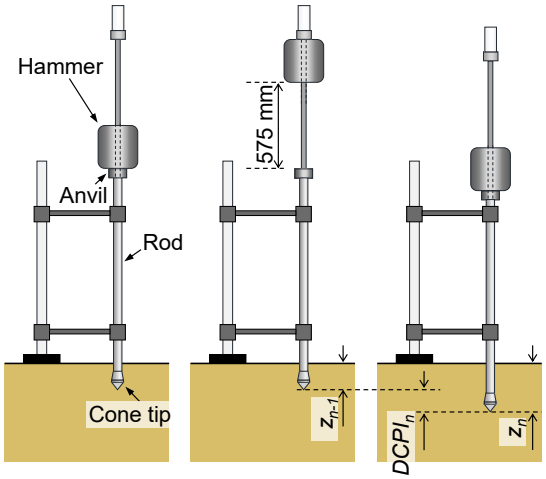

Fig. 4 Dynamic cone penetrometer

$$\mathrm{DCPI}_n = d_n - d_{n-1} \tag{5}$$

where DCPI_n represents the penetration index calculated at the n-th blow, while d_n and $d_{n\text{-}1}$ denote the cumulative penetration depths after the n-th and $(n-1)$-th hammer drops, respectively, as shown in Fig. 4.

3. Experimental study

3.1 Site description

The experimental site was established in an open field in

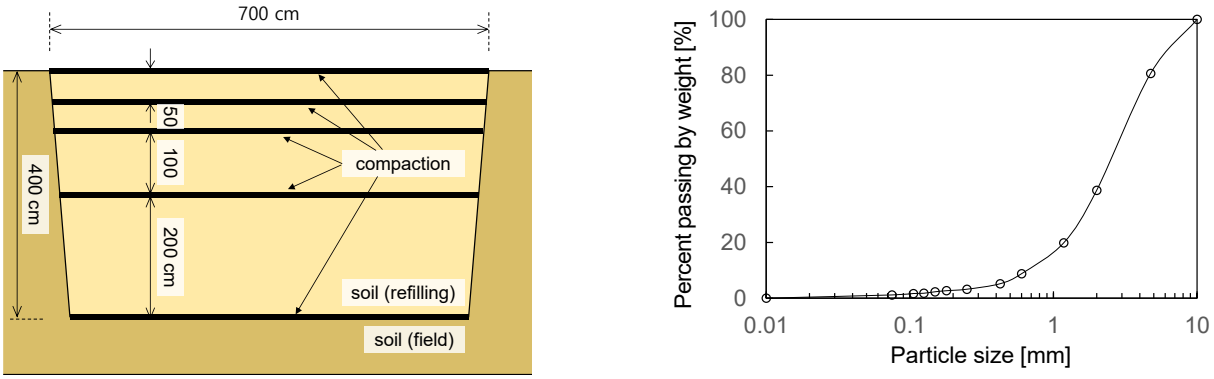

(a) Side view of testbed (b) Particle size distribution of testbed

Fig. 5 Testbed construction

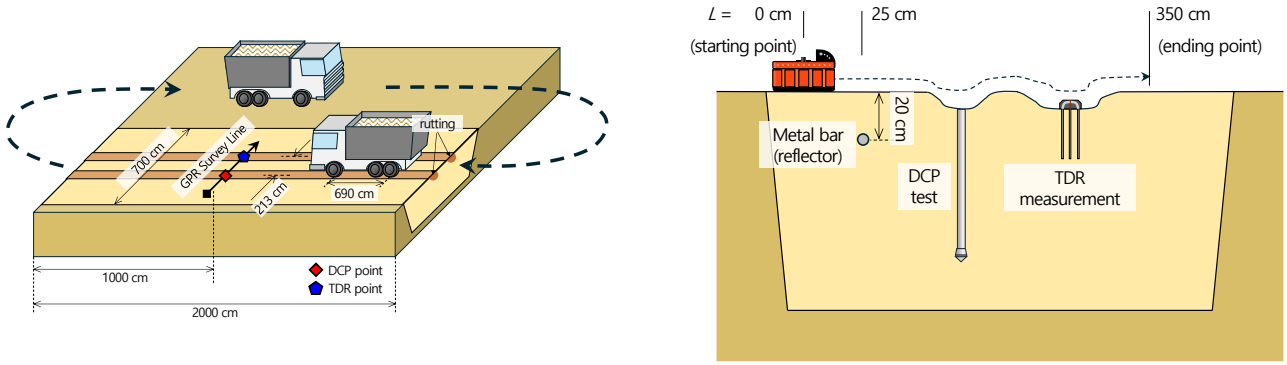

(a) Vehicular loading on testbed (b) Measurement location

Fig. 6 Experimental setup

Pocheon, Republic of Korea. A testbed simulating an unpaved road was constructed by excavating a straight trench with a maximum depth of 400 cm and width of up to 700 cm, as shown in Fig. 5(a). Consequently, the trench was refilled with the original soil material. The testbed consisted of four layers: the first and second layers were located at d = 200–400 cm and d = 100–200 cm, respectively; the third and fourth layers were positioned at d = 50–100 cm and d = 0–50 cm, respectively. A 24-ton roller compactor was used to compact each layer. Consequently, soil compaction was conducted at depths of d = 0 mm, 50 mm, 100 mm, 200 mm, and 400 mm, as shown in Fig. 5(a). The particle size distribution of the site soil is shown in Fig. 5(b). According to the Unified Soil Classification System (USCS), the soil is classified as poorly graded sand (SP).

3.2 Experimental setup

Vehicular loading was conducted on the testbed by operating a dump truck weighing 147 kN along a circular loop track, a portion of which included the testbed, as shown in Fig. 6(a). The truck was driven around this loop after 0, 100, 200, and 500 passes at a consistent speed of 30 km/h, thereby directly applying repeated vehicular loads to the testbed surface. This method was designed to replicate the progressive ground deformation induced by repeated traffic loading. The dump truck used in this study was 690 cm in length and 213 cm in width.

A GPR survey was conducted across the testbed to evaluate the surface deformation resulting from vehicular loading, as shown in Fig. 6(b). The GPR signals were collected after each loading stage, producing four datasets corresponding to 0, 100, 200, and 500 passes. For an accurate alignment of the GPR antenna during the measurements, a short metal bar (length = 20 cm) was embedded at L = 25 cm on the GPR survey line to serve as a reference marker in the GPR image (Fig. 6(b)). The scan rate of the GPR survey was set to 400 scans/m, and the total length of the survey line was 350 cm. Accordingly, 1,400 GPR signals were acquired along the entire survey line. All GPR surveys were conducted using a shielded 350 MHz antenna (GSSI, 350 HS Antenna).

In addition, both the TDR and DCP tests were conducted at a single point where the rutting lines formed by the dump truck intersected the GPR survey line, as shown in Fig. 6. The TDR measurements were performed after 0, 100, 200, and 500 passes of the dump truck, whereas the DCP tests were performed after 0, 100, and 500 passes. Accordingly, a total of four TDR signals and three DCPI profiles were obtained. TDR data were collected to enhance the accuracy of the depth estimations derived from the GPR measurements. The TDR measurements were performed using a TDR analyzer (Hyperlabs, HL1101). In parallel, the DCPI profiles were acquired to assess the absolute ground deformation at each loading stage by estimating the depths of the subsurface interfaces.

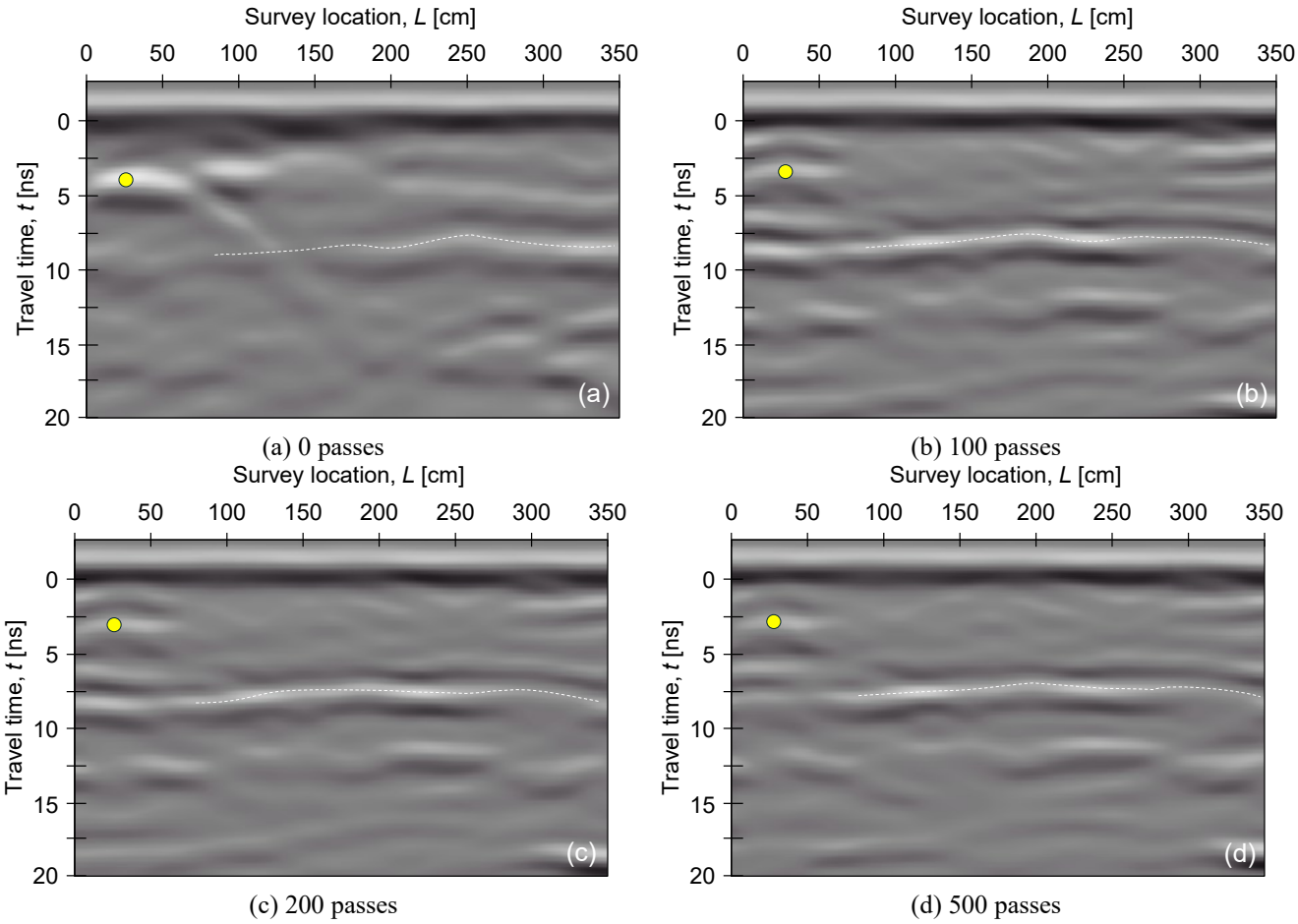

(a) 0 passes (b) 100 passes

(c) 200 passes (d) 500 passes

Fig. 7 GPR signals obtained after dump truck passes

3.3 Experimental results

3.3.1 GPR images

The measured GPR images are shown in Fig. 7. In all four GPR images shown in Fig. 7, two common features were observed: (1) linear patterns in B–W–B polarity near t = 0 ns across the entire survey location; and (2) parabolic patterns in W–B–W polarity at approximately t = 3.5 ns, extending from L = 0–50 cm. The linear patterns were identified as direct waves (Hoang *et al*. 2024a, Hoang *et al*. 2024b), which were used as a reference for the polarity comparison, whereas the parabolic patterns were interpreted as the location of the metal bar (yellow circles in Fig. 7) buried as a reference marker. Note that metallic materials have infinite permittivity (Daniels 2007, Everett 2013), which generally causes the reflected wave from a rebar to have opposite polarity to that of the incident wave (Kang *et al*. 2022, Kang *et al*. 2024). In addition, all four GPR images exhibited B–W–B polarity patterns (white dashed lines in Fig. 7) within t = 7.5–10 ns, extending from L = 50–350 cm. Significant rutting caused by both truck wheels was observed near the GPR survey locations L = 200 cm and L = 320 cm. Accordingly, the rutting lines where the TDR measurements and DCP tests were performed were located near L = 200 cm and L = 320 cm in the GPR images.

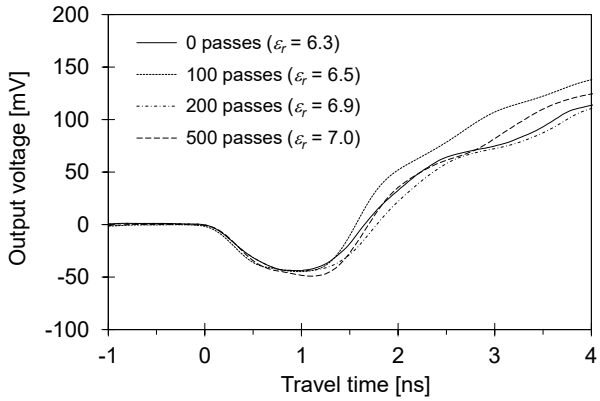

Fig. 8 Measured TDR signals

3.3.2 TDR signals

Fig. 8 shows the TDR signals obtained after each loading stage. Because the rutting line could not be identified prior to the dump truck loading, the TDR measurement for the 0-pass case was conducted at L = 175 cm. Subsequently, the TDR measurements for the remaining cases were conducted at L = 315 cm. Each TDR signal exhibits a point where the initially constant value of zero begins to decrease; these points are referred to as the first inflection points. To ensure consistent comparison, the first inflection point of each signal was set to 0 ns, and all

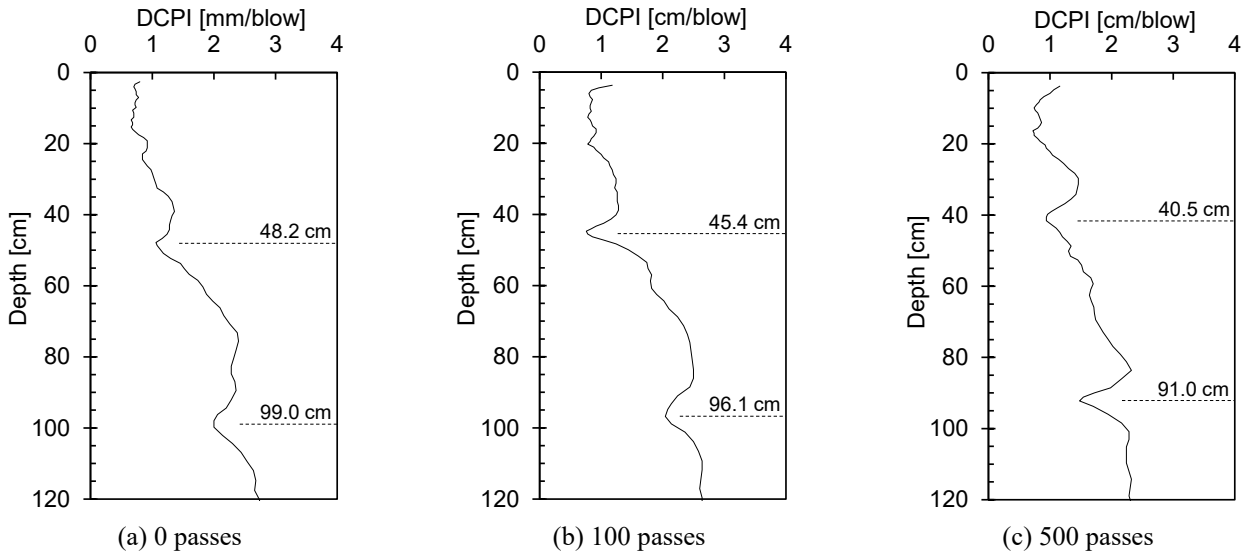

(a) 0 passes (b) 100 passes (c) 500 passes

Fig. 9 DCPI profiles obtained after dump truck passes

signals were realigned accordingly. Following the first inflection point, the signals gradually decreased until they reached the second point, where the trend reversed and the signals began to increase, as shown in Fig. 8. These points, which were identified using the tangent method, were defined as the second inflection points. The second inflection point appeared at progressively longer travel times, as the number of dump truck passes increased. The ε_r values for each case were estimated from the TDR signals using Eq. (4), yielding values of ε_r = 6.3, 6.5, 6.9, and 7.0 for 0, 100, 200, and 500 passes, respectively. The results are summarized in the insets of Fig. 8.

3.3.3 DCPI profiles

Fig. 9 shows the DCPI profiles acquired after 0, 100, and 500 passes by using the dump truck. Because the rutting line could not be identified prior to loading with the dump truck, the DCP test for the 0-pass case was performed at L = 260 cm. In addition, after the vehicular loading, distinct rutting was observed at approximately L = 185–225 cm. Therefore, the DCP tests for the 100- and 500-pass cases were conducted at L = 205 cm. In the 0-pass case (Fig. 9(a)), the DCPI exhibited a gradually increasing trend from the surface to a depth of 120 cm. However, DCPI values decreased around depths of 48.2 cm and 98.8 cm. Similarly, the DCPI profiles for the 100-pass and 500-pass cases showed a gradual increase with depth, with reductions occurring at two separate depths for each case (Fig. 9). The two interface depths at which the DCPI values decreased for all three cases are summarized in the insets of Fig. 9 and Table 1.

4. Analyses and discussion

4.1 Identification of subsurface interface in GPR images

The patterns observed within t = 7.5–10 ns and extending along L = 50–350 cm, delineated by the white dashed lines in Fig. 7, exhibit a B–W–B polarity. This polarity corresponds to a negative reflection coefficient, indicating that the ε_r of the upper layer is lower than that of the underlying layer, as described in Eq. (2). Because ε_r increases with increasing relative density (Kang *et al*. 2023, Kang *et al*. 2025b, Rasch 2011), the B–W–B patterns were interpreted as representing one of the four layer interfaces that were compacted using a roller compactor during the testbed construction.

Considering the overlap with the hyperbolic patterns induced by the metal bar, the travel times of the patterns in the B–W–B polarity were extracted within the range of L = 100–350 cm. Because the scan rate was set to 400 scans per meter, extraction was conducted on 1,000 GPR signals. The extracted travel times are presented in Fig. 10(a).

4.2 Depth estimation of subsurface interface

As the relative density of the testbed surface may vary depending on the number of dump truck passes, the corresponding ε_r values may be nonuniform (Rasch 2011). Based on Eq. (3), the extracted travel times (Fig. 10(a)) were converted into interface depths using the ε_r values obtained from TDR measurements for each pass count case. The calculated interface depths within the range of L = 100–350 cm are presented in Fig. 10(b). The results for the 0-pass case indicate that the subsurface interface is generally located at approximately d = 50–55 cm across most of the GPR survey lines. However, a localized shallow interface was observed within L = 200–300 cm, which was attributed to nonuniform soil compaction. As shown in Fig. 10(b), the 100, 200, and 500-pass cases all exhibit the shallowest interface depths of approximately L = 200–210 cm. Subsequently, a slight increase in the depth was observed in all three cases up to L = 260 cm, followed by a slight decrease at L = 300 cm. At L = 320 cm, the interface depth increases sharply. Note that the DCP tests were conducted at L = 260 cm for the 0-pass case and at L = 205

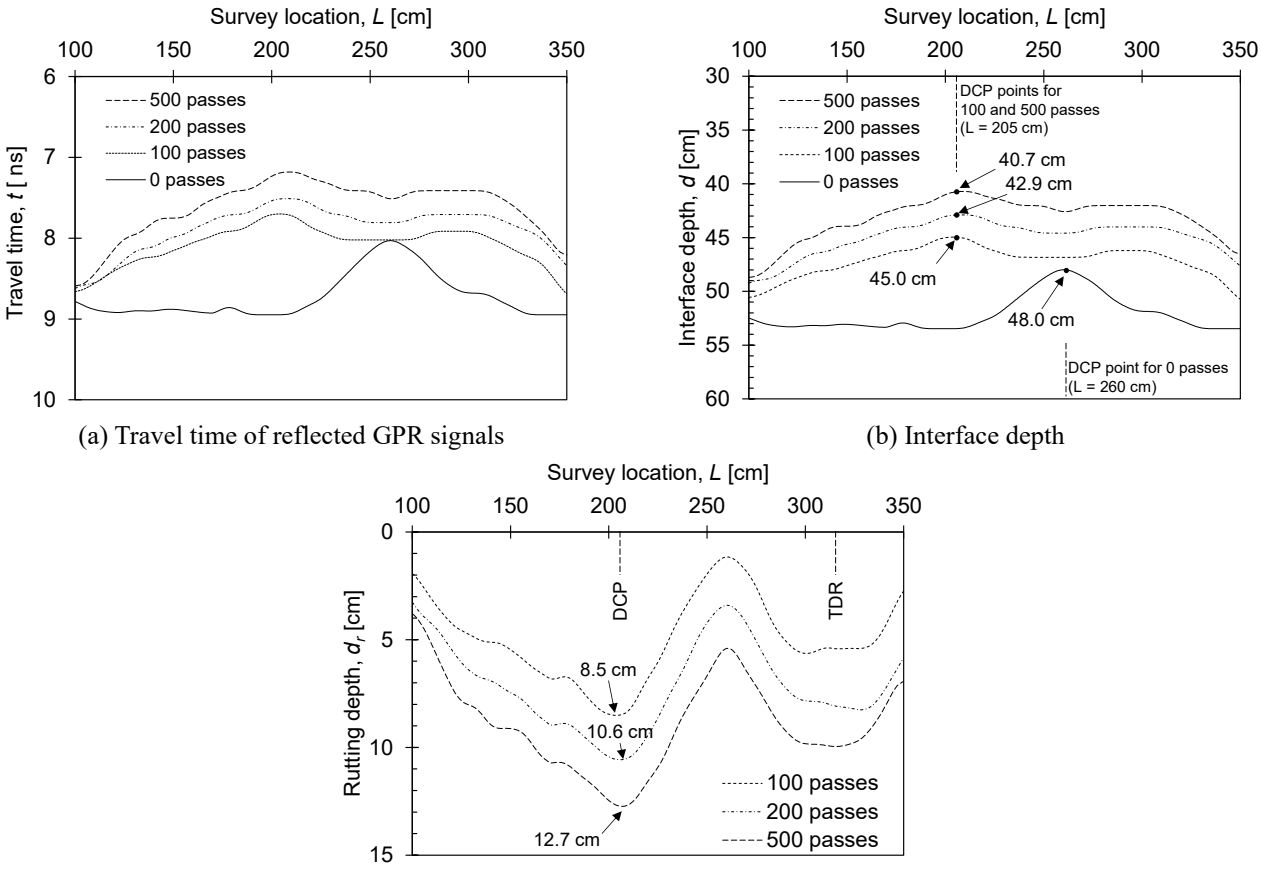

(a) Travel time of reflected GPR signals

(b) Interface depth

(c) Rutting depth across entire road cross section

Fig. 10 Rutting depth calculation

Table 1 Subsurface interface depth from DCPI profiles and GPR-based analysis (Unit: cm)

		0 passes	100 passes	200 passes	500 passes
DCPI Profiles	First Interface	48.2	45.4	-	40.5
	Second Interface	98.8	96.1	-	91.0
	Depth Difference	50.6	50.7	-	50.5
GPR-based (at L = 210 cm)		48.0	45.0	42.9	40.7
Difference		0.2	0.4	-	0.2

Table 2 Maximum rutting depth estimated from GPR-based and conventional methods (Unit: cm)

	100 passes	200 passes	500 passes
GPR-based (at L = 210 cm)	8.5	10.6	12.7
Straightedge Method	6.8	7.1	7.5
Difference	1.7	3.5	5.2

cm for the 100- and 500-pass cases. The interface depths estimated from the GPR signals at each location were 48.0 cm, 45.0 cm, and 40.7 cm, respectively, as shown in the insets of Fig. 10(b). These values correspond to the depths at which a decrease in DCPI values was observed in the DCPI profiles (Fig. 9), indicating that the interface depth estimations using GPR and TDR are highly accurate. The interface depths estimated by GPR-based analysis are summarized in Table 1.

However, to evaluate the rutting depth induced by vehicular loading, it is necessary to assess the deviation from the 0-pass case. Accordingly, the rutting depth d_r was calculated at each survey location by measuring the difference between the interface depths of the 100-, 200-, and 500-pass cases and that of the 0-pass case. The results are presented in Fig. 10(c). Fig. 10(c) shows that the maximum d_r values were observed at approximately L = 210 cm for all three cases. In addition, significant d_r values were observed at approximately L = 320 cm. The maximum d_r values derived from the GPR-based analysis for each pass count are summarized in the insets of Fig. 10(c) and Table 2. Furthermore, as the number of dump truck passes increased, deformations were concentrated at L = 210 cm and L = 320 cm as well as appeared at other locations, as shown in Fig. 10(c). The dump truck was operated in a loop rather than in a back-and-forth manner. Consequently, the spatial distribution of deformations across the entire survey line was considered to be influenced by the vehicle wandering effect (Hui *et al*. 2018, Yang *et al*. 2023, Yang *et al*. 2024). This effect also explains why the spacing between the rutting lines observed on the testbed surface did not match the tire spacing of the dump truck (213 cm) in this

study (Fig. 6(a)).

4.3 Validation of GPR-based interface depth estimation using DCPI profiles

According to Fig. 9 and Table 1, two apparent subsurface interfaces were identified from the DCPI profiles in all cases of 0, 100, and 500 dump truck passes: the first interface was at a depth of less than 50 cm, and the second was between 90 and 100 cm. The depth difference between them was approximately 50 cm in all cases as shown in Table 1. Based on this observation, these interfaces were considered to correspond to the boundaries between the third and fourth compacted layers, and between the second and third layers (Fig. 5(a)). Thus, the first interface from the DCPI profiles corresponds to the target interface identified by the GPR-based analysis. The GPR results were compared to the corresponding depths obtained from the DCPI profiles to assess the accuracy of the GPR-estimated depths. As shown in Table 1, the difference between the two methods was less than 0.4 cm in all cases, indicating that the GPR-based analysis reliably captured the actual subsurface interface depth across the survey line.

4.4 Comparison between GPR-based and conventional rutting depth estimation methods

The rutting depths were measured using the straightedge method (ASTM E1703 2010) for 0, 100, and 500 dump truck passes. The results were compared with the rutting depths estimated from the GPR-based analysis. As shown in Fig. 10(c) and Table 2, the maximum d_r values obtained from the GPR-based method were 8.5, 10.6, and 12.7 cm for the 100, 200 and 500 pass cases, respectively. In contrast, the corresponding values measured using the conventional method were 6.8, 7.1, and 7.5 cm, indicating that the GPR-based method yielded consistently higher rutting depth estimates across all cases. Moreover, the difference between the two methods increases with the number of dump truck passes. This increasing difference is attributed to the spatial distribution of deformations caused by the vehicle wandering effect. Rutting depth can serve as an important indicator for evaluating the serviceability of unpaved roads. The conventional method relies on the crests on both sides of the rut. However, due to the vehicle wandering effect, these crests may also settle, potentially leading to an underestimation of the actual rutting depth. In contrast, the GPR-based analysis in this study estimates rutting depth by evaluating changes in thickness between subsurface layers, thereby minimizing the influence of crest settlement. Consequently, the proposed method is expected to provide a more reliable assessment of pavement serviceability. Furthermore, this study utilized relative permittivity values estimated from TDR signals measured at the soil surface to assess the feasibility of evaluating rutting depth using both TDR and GPR techniques. The use of a penetrable TDR sensor, which can account for variations in permittivity with depth (Hong *et al*. 2019, Kang *et al*. 2025b), may reduce the error between the evaluated and actual rutting depths.

5. Conclusions

This study explored the application of GPR and TDR to evaluate rutting depth on unpaved roads. A dump truck was driven along a circular track with an unpaved road testbed incorporated as a section of the loop, following 0, 100, 200, and 500 passes. GPR surveys were conducted to capture the distribution of rutting across the entire testbed, and the rutting depths were estimated using the relative permittivities obtained from the TDR measurements. The accuracy of the estimated rutting depths was validated by comparing them with the interface depths obtained from the DCP tests. In addition, the results of the GPR-based analysis were compared with the rutting depths measured using a conventional straightedge method. The remarkable observations are as follows:

• Contrarily to the conventional method, which only measures the maximum rutting depth, the combined use of GPR and TDR enables the evaluation of the rutting distribution across the entire road cross section and allows for an accurate estimation of the rutting depth.

• Compared with conventional methods, GPR-based analysis tends to estimate greater rutting depths. This is because while the GPR-based approach uses the underlying ground layer as a reference, which is relatively less affected by surface-applied loading, the conventional method using a straightedge relies on the crests on both sides of the rut. These crests may settle owing to deformation, causing an underestimation of the rutting depth.

• The GPR and TDR techniques employed in this study are robust tools for evaluating the rutting depth across an entire road cross section.

Acknowledgments

This work was supported by the National Research Foundation of Korea (NRF) grant funded by the Korea government (MSIT) (RS-2021-NR060085).

References

Abbondati, F., Biancardo, S.A., Veropalumbo, R. and Dell'Acqua, G. (2021), "Surface monitoring of road pavements using mobile crowdsensing technology", *Measurement*, **171**, 108763. https://doi.org/10.1016/j.measurement.2020.108763.

Aleadelat, W., Wright, C.H. and Ksaibati, K. (2018), "Estimation of gravel roads ride quality through an android-based smartphone", *Transp. Res. Record*, **2672**(40), 14-21. https://doi.org/10.1177/0361198118758693.

Annan, A.P. (2003), Ground Penetrating Radar Principles, Procedures and Applications, Sensors and Software Inc., Mississauga, ON, Canada.

ASTM D6565 (2005), *Standard Test Method for Determination of Water (Moisture) Content of Soil by the Time-Domain Reflectometry (TDR) Method, ASTM International*, West Conshohocken, PA, USA.

ASTM D6951 (2009), *Standard Test Method for Use of the*

Dynamic Cone Penetrometer in Shallow Pavement Applications, ASTM International, West Conshohocken, PA, USA.

ASTM E1703 (2010), *Standard Test Method for Measuring Rut-Depth of Pavement Surfaces Using a Straightedge*, ASTM International, West Conshohocken, PA, USA.

Daniels, D.J. (2004), *Ground Penetrating Radar (Vol. 1)*. Iet, London, UK.

Davis, J.L. and Annan, A.P. (1989), "Ground-penetrating radar for high-resolution mapping of soil and rock stratigraphy 1", *Geophys. Prospect.*, **37**(5), 531-551. https://doi.org/10.1111/j.1365-2478.1989.tb02221.x.

Eaton, R.A. (1992), *Unsurfaced Road Maintenance Management, US Army Corps of Engineers*, Cold Regions Research & Engineering Laboratory, USA.

Everett, M.E. (2013), *Near-Surface Applied Geophysics*. Cambridge University Press, Cambridge, UK.

Hausmann, M.R. (1987), "Geotextiles for unpaved roads—a review of design procedures", *Geophys. Prospect.*, **5**(3), 201-233. https://doi.org/10.1016/0266-1144(87)90017-3.

Heidari, M.J., Najafi, A. and Borges, J.G. (2022), "Introducing new index in forest roads pavement management system", *Forests*, **13**(10), 1674. https://doi.org/10.3390/f13101674.

Hoang, N.Q., Kang, S., Yoon, H.K. and Lee, J.S. (2024a), "Enhancing anomaly detection in ground-penetrating radar images through reconstruction loss and high-variability", *Results Eng*., **21**, 101874. https://doi.org/10.1016/j.rineng.2024.101874.

Hoang, N.Q., Shim, S., Kang, S. and Lee, J.S. (2024b), "Anomaly detection via improvement of GPR image quality using ensemble restoration networks", *Autom. Constr*., **165**, 105552. https://doi.org/10.1016/j.autcon.2024.105552.

Hong, W.T. and Lee, J.S. (2018), "Estimation of ground cavity configurations using ground penetrating radar and time domain reflectometry", *Nat. Haz.*, **92**, 1789-1807. https://doi.org/10.1007/s11069-018-3278-z.

Hong, W.T., Jung, Y.S., Kang, S. and Lee, J.S. (2016), "Estimation of soil-water characteristic curves in multiple-cycles using membrane and TDR system", *Materials*, **9**(12), 1019. https://doi.org/10.3390/ma9121019.

Hong, W.T., Kang, S., Lee, S.J. and Lee, J.S. (2018), "Analyses of GPR signals for characterization of ground conditions in urban areas", *J. Appl. Geophys.*, **152**, 65-76. https://doi.org/10.1016/j.jappgeo.2018.03.005.

Hong, W.T., Yu, J.D., Kim, S.Y. and Lee, J.S. (2019), "Dynamic cone penetrometer incorporated with time domain reflectometry (TDR) sensors for the evaluation of water contents in sandy soils", *Sensors*, **19**(18), 3841. https://doi.org/10.3390/s19183841.

Hui, B., Tsai, Y.J., Guo, M. and Liu, X. (2018), "Critical assessment of the impact of vehicle wandering on rut depth measurement accuracy using 13-point based lasers", *Measurement*, **123**, 246-253. https://doi.org/10.1016/j.measurement.2018.03.069.

Jia, W., Wang, S., Min, S. and Zhang, Y. (2022), "Electromagnetic energy focusing technology with GPR array transmitting antenna for high resolution detection", *Measurement*, **203**, 112000. https://doi.org/10.1016/j.measurement.2022.112000.

Jiao, L., Ye, Q., Cao, X., Huston, D. and Xia, T. (2020), "Identifying concrete structure defects in GPR image", *Measurement*, **160**, 107839. https://doi.org/10.1016/j.measurement.2020.107839.

Kang, S., Yu, J.D., Hong, W.T. and Lee, J.S. (2021), "Estimation of cavities beneath plate structures using a microphone: laboratory model tests", *Sensors*, **21**(9), 2941. https://doi.org/10.3390/s21092941.

Kang, S., Yu, J.D., Han, W. and Lee, J.S. (2022), "Nondestructive detection of cavities beneath concrete plates using ground penetrating radar and microphone", *NDT E Int.*, **130**, 102663. https://doi.org/10.1016/j.ndteint.2022.102663.

Kang, S., Lee, J.S., Park, G., Kim, N. and Park, J. (2023), "Unpaved road characterization during rainfall scenario: Electromagnetic wave and cone penetration assessment", *NDT E Int.*, **139**, 102930. https://doi.org/10.1016/j.ndteint.2023.102930.

Kang, S., Lee, J.S., Kim, N., Lee, D. and Park, J. (2024), "Detection of air-and water-filled cavities beneath concrete plate using electromagnetic and acoustic waves" *NDT E Int.*, **144**, 103103. https://doi.org/10.1016/j.ndteint.2024.103103.

Kang, S., Yu, J.D., Lee, D. and Lee, J.S. (2025a), "Investigating the unbonded sections of fully grouted rock bolts using a microphone", *Transp. Geotech*., **51**, 101488. https://doi.org/10.1016/j.trgeo.2025.101488.

Kang, S., Park, G., Kim, N., Tutumluer, E. and Lee, J.S. (2025b), "GPR-based depth estimation of ground interfaces in permafrost region: Electromagnetic method and cone penetration assessment", *Measurement*, **242**, 116158. https://doi.org/10.1016/j.measurement.2024.116158.

Kim, S.Y., Kang, S., Park, G., Lee, D., Lim, Y. and Lee, J.S. (2024), "Detection of roadbed layers in mountainous area using down-up-crosshole penetrometer and ground penetrating radar", *Measurement*, **224**, 113889. https://doi.org/10.1016/j.measurement.2023.113889.

Kim, Y., Jafri, T.H. and Do, J. (2025), "Effect of geocell height on behavior of sand under constant compaction energy evaluated by plate load testing in large-scale soil box", *Int. J. Geo-Eng.*, **16**(1), 1. https://doi.org/10.1186/s40703-024-00226-0.

Klemunes Jr, J. (1998), "Determining Soil Volumetric Moisture Content using Time Domain Reflectometry", No. FHWA-RD-97-139; U.S. Dept. of Transportation, Federal Highway Administration, Research and Development, Turner-Fairbank Highway Research Center.

Korea Transport Institute (2019), *A study of the Adequacy Assessment of Road Infrastructure and Investment Direction*, Korea Transport Institute, South Korea.

Ministry of Land, Infrastructure and Transport (MOLIT) of Korea (2022), *2021 YEARBOOK OF ROAD STATISTICS*, MOLIT, South Korea.

Ramjiram Thakur, S., Naveen, B.P. and Tegar, J.P. (2021), "Improvement in CBR value of soil reinforced with nonwoven geotextile sheets", *Int. J. Geo-Eng.*, **12**(1), 8. https://doi.org/10.1186/s40703-020-00138-9.

Rasch, S.M. (2011), "Determining the relative effects of volumetric water content and dry density on the dielectric constant of soils", University of Missouri-Columbia.

Santamarina, J.C., Klein, A. and Fam, M.A. (2001), "Soils and waves: Particulate materials behavior, characterization and process monitoring", *J. Soils Sediments*, **1**(2), 130-130. https://doi.org/10.1007/BF02987719.

Scala, A.J. (1956), "Simple methods of flexible pavement design using cone penetrometers", *New Zealand Eng.*, **11**(2), 34-44. https://search.informit.org/doi/10.3316/informit.218423931293630.

Soria, M.H. and Fontenele, E.B. (2003), "Field evaluation of method for rating unsurfaced road conditions", *Transp. Res. Record*, **1819**(1), 267-272. https://doi.org/10.3141/1819a-39.

Wang, D., Falchetto, A.C., Goeke, M., Wang, W., Li, T. and Wistuba, M.P. (2017), "Influence of computation algorithm on the accuracy of rut depth measurement", *J. Traffic Transp. Eng.-Engl. Ed.*, **4**(2), 156-164. https://doi.org/10.1016/j.jtte.2017.03.001.

Yang, X., Wang, X., Podolsky, J., Huang, Y. and Lu, P. (2023), "Assessing vehicle wandering effects on the accuracy of weigh-in-motion measurement based on in-pavement fiber Bragg

sensors through a hybrid sensor-camera system", *Sensors*, **23**(21), 8707. https://doi.org/10.3390/s23218707.

Yang, X., Wang, X., Podolsky, J., Huang, Y. and Lu, P. (2024), "Addressing wander effect in vehicle weight monitoring: An advanced hybrid weigh-in-motion system integrating computer vision and in-pavement sensors", *Measurement*, **234**, 114870. https://doi.org/10.1016/j.measurement.2024.114870.

Yelf, R. (2004), "Where is true time zero?", *Proceedings of the Tenth International Conference on Grounds Penetrating Radar 2004*, Delft, Netherlands, June.